# On Analytical Study of Self-Affine Maps

M. Saadatmand-Tarzjan[1]                H. Ghassemian[2]

[1] Assistant Prof., Medical Imaging Lab, Department of Electrical Engineering, Ferdowsi University of Mashhad, Mashhad, Iran
saadatmand@um.ac.ir

[2] Prof., Department of Electrical Engineering, Tarbiat Modares University, Tehran, Iran
ghassemi@modares.ac.ir

## Abstract :

Self-affine maps were successfully used for edge detection, image segmentation, and contour extraction. They belong to the general category of patch-based methods. Particularly, each self-affine map is defined by one pair of patches in the image domain. By minimizing the difference between these patches, the optimal translation vector of the self-affine map is obtained. Almost all image processing methods, developed by using self-affine maps, take advantage of either the attracting or repelling behaviors which have been, only, experimentally investigated. In this paper, we analytically study the properties of self-affine maps and prove their attracting and repelling behaviors. Furthermore, the new corner/edge pointing behavior is also proposed for contractive self-affine maps. We show that the conventional cost function of self-affine maps may cause critical uncertainty due to providing multiple equivalent optimal translation vectors. Thus, a new cost function is suggested to effectively tackle this problem. For evaluation, it is used with the self-affine snake (SAS) for contour extraction. Experimental results demonstrated that the enhanced SAS provides better performance compared to a number of different active contour methods in terms of both solution quality and CPU time.

**Keywords:** Patch-Based Image Processing, Self-Affine Map, Analytical Study, Image Segmentation, Contour Extraction.

# 1. Introduction

Patch-based techniques are widely used in image analysis, image processing, and image synthesis. Although patches are simply defined as local neighborhoods centered at image components, they have intrinsic capabilities to maintain large-scale structures and textures of natural images. Furthermore, patch-based methods may be intuitively similar to those human vision tasks which compare semi-local image neighborhoods. Despite outstanding performance, they are often simple to implement.

For example, estimation of the displacement field between two images is a well-known classical problem which can be addressed by the frequently-used block matching algorithm [1-3]. In this approach, every patch of one image is compared to all candidate patches of the other one to find the best similarity. Another example is the sophisticated problem of synthesizing a texture similar to a specified model [4-6]. It was effectively tackled by an iterated copy-paste procedure of different patches given from the model. Some variants of such techniques were also employed by texture transferring [7-8], textured-inpainting [9-11], and image completion [12-13].

It is also worth citing recent patch-based denoising methods [14-20]. The conventional denoising algorithms generally restore each component value by computing a weighted average of neighboring components values [21-24]. Buades *et al.* [14] explained that comparing only components values is not robust enough. They proposed the non-local means (NL-means) algorithm which iteratively evaluates the photometric similarity of patches centered at neighboring components to obtain weighting coefficients. Kervrann and Boulanger [25] extended NL-means by employing adaptive neighborhoods which balance both approximation accuracy and stochastic error at each spatial position. Besides, Gilboa and Osher [26] defined the variational formulation of NL-means by using a non-local partial differential equation. Recently, Azzabou *et al.* [15] and Tschumperlé-Brun [27] incorporated spatial and photometric similarities through different variational formulations. The former used scale adaptive kernels while the later defined a new patch space.

Non-local region-based active contours (RBACs) are other elegant instances of patch-based approaches. Conventionally, RBACs (*e.g.* region competition [28], geodesic active region [29], and piecewise constant model [30]) use statistical descriptors and homogeneity conditions for specifying each region of interest to guide evolution of the curve [31]. Despite promising results, they may fail to segment images with texture, inhomogeneous intensity, or heterogeneous objects. Recently, patch-based variational formulations were proposed as a solution to this problem [32-34]. They compute statistical descriptors of each region by using image patches instead of exact values of its components. For example, Li *et al.* [32, 33] employed the image patches defined by Gaussian kernels to locally approximate image intensities on each side of the contour. In another work, Lankton and Tannenbaum [34] proposed a local region-based framework based on ball-shaped patches. They integrated the framework with the uniform modeling [30], mean separation [35], and histogram separation [36] energies to provide considerable improvements.

Texture classification [37], background estimation [38], compression artifacts removal [39], and medical image indexing and retrieval [40] are some other examples of patch-based image processing and analysis methods proposed by researchers.

However, self-affine maps naturally differ from the aforementioned methods. Generally, each self-affine map is defined by a pair of the domain and range patches in the image domain. The parameters of a self-affine map are obtained by maximizing a similarity measure between its patches. Self-affine maps provided promising results in different applications such as producing fractal figures [41, 42] and fractal image coding [43]. Furthermore, Ida and Sambonsugi [44] showed that image edges can attract the components which are iteratively mapped through contractive self-affine maps (CSAMs) while expanding self-affine maps (ESAMs) repel them from edges. They employed the above phenomena to provide a number of image processing algorithms such as edge detection and image segmentation. In another work, they used CSAMs for contour extraction in order to closely fit self-affine curves to the desired object boundaries [45]. However, the curve sometimes abnormally deformed due to the fractal behavior. The authors tackled this problem by defining the contour as a primary parametric curve [46]. Recently, they progressed to the self-affine snake (SAS) which integrates self-affine maps, wavelet transform, and parametric active contours [47, 48]. However, all of the above promising methods were mainly developed based on Ida and Sambonsugi's primary work (about the attracting and repelling behaviors of self-affine maps) with no analytical justification.

In this paper, we analytically study properties of self-affine maps by providing five lemmas and two theorems. It is proved that CSAMs/ESAMs usually provide optimal translation vectors which support the attracting/repelling behavior. Furthermore, we establish the new corner/edge pointing (CEP) behavior. It states that every optimal translation vector of a CSAM usually points toward a corner or an edge in the image. All of these consequences further justify the image processing algorithms previously proposed by researchers based on experimentally-validated self-affine maps' properties. Besides, the traditional cost function of self-affine maps suffers the problem of non-unique optimal solution. We propose a new cost function to effectively tackle it. According to

experimental results, the performance of SAS was improved by using the proposed cost function.

The paper is organized as follows. In Section 2, analytical principles of self-affine maps are exhaustively stated. Furthermore, the new corner/edge pointing behavior is also proposed in this section. Experimental results on enhanced SAS performance is presented in Section 3. Finally, Section 4 is devoted to conclusion remarks.

The notations used in this paper are fairly standard. Matrices are shown by upper-case letters while boldface symbols are used for vectors in lower-case letters. We also have the following notations:

| | |
|---|---|
| $I(\boldsymbol{x})$ | Gray-level of the image at the position $\boldsymbol{x}$ |
| M | The domain patch of a self-affine map |
| W | The range patch of a self-affine map |
| $m(.)$ | Contractive affine mapping function |
| $\omega(.)$ | Expanding affine mapping function |
| $r_m$ | Scaling coefficient of CSAM |
| $r_\omega$ | Scaling coefficient of ESAM |
| $\boldsymbol{x}_\omega$ | A component of W |
| $\boldsymbol{x}_m$ | A component of M |
| $\bar{\boldsymbol{x}}_m$ | The center point of M |
| $\bar{\boldsymbol{x}}_\omega$ | The center point of W |
| $e_W$ | Self-affine cost function defined over W |
| $e_M$ | Dual of the self-affine cost function defined over M |
| $\boldsymbol{\tau}$ | A translation vector |
| $\tilde{\boldsymbol{\tau}}$ | Optimal translation vector |
| $\nabla_x$ | Gradient operator with respect to $\boldsymbol{x}$ |
| $\nabla_\tau$ | Gradient operator with respect to $\boldsymbol{\tau}$ |
| $L_i$ | The $i$th edge-segment |
| $T_i$ | The locus line of locally optimal translation vectors corresponding to $L_i$ |
| $C_i$ | The locus line of locally optimal W-centers corresponding to $L_i$ |

Furthermore, we use the following abbreviations:

| | |
|---|---|
| ACWE | Active contour without edges |
| CEP | Corner/edge pointing |
| CSAM | Contractive self-affine map |
| ES | Edge-segment |
| ESAM | Expanding self-affine map |
| G0TV | Globally optimal translation vector with zero cost value |
| G0WC | Globally optimal W-center with zero cost value |
| GOTV | Globally optimal translation vector |
| GOWC | Globally optimal W-center |
| GVF | Gradient vector flow |
| GGVF | Generalized gradient vector flow |
| LLT | The locus-line of optimal translation vectors |
| LLW | The locus-line of optimal W-centers |
| LOTV | Locally optimal translation vector |
| LOWC | Locally optimal W-center |
| PC | Piecewise constant |
| SAS | Self-affine snake |

## 2. Analytical Principles

In this section, we exhaustively analyze the performance of self-affine maps. In more detail, first, the fundamentals of self-affine maps are briefly introduced (Subsection 2.1). Then, the relationship between the self-affine cost function and Mumford-Shah functional is stated (Subsection 2.2). Next, the obvious solution of the cost function is obtained (Subsection 2.3). Afterwards, the global zero-minima of the cost function are computed (Subsection 2.4). Then, some important local minima of the cost function are obtained (Subsection 2.5). Finally, we proposed a novel cost function for self-affine maps based on the new corner/edge pointing behavior (Subsection 2.6).

### 2.1. Self-Affine Maps

Consider an image having the domain $\Omega \subset R^2$ with the gray-level $I(\boldsymbol{x}) \in [0,1]$ for all $\boldsymbol{x}=(x,y) \in \Omega$. The CSAM $m:M \to W$ is defined as follows:

$$\boldsymbol{x}_\omega = m(\boldsymbol{x}) = r_m(\boldsymbol{x} - \bar{\boldsymbol{x}}_m) + \bar{\boldsymbol{x}}_\omega, \quad r_m < 1 \qquad (1)$$

where $\bar{\boldsymbol{x}}_m = (\bar{y}_m, \bar{x}_m)$ and $\bar{\boldsymbol{x}}_\omega = (\bar{y}_\omega, \bar{x}_\omega)$ are center points of the domain-patch M and range-patch W (both $\subset \Omega$), respectively, such that:

$$\bar{\boldsymbol{x}}_\omega = \bar{\boldsymbol{x}}_m + \boldsymbol{\tau} \qquad (2)$$

where $\boldsymbol{\tau}=(s,t)$ is a translation vector. In other words, the CSAM of Eqn. (1) contracts M by the scaling coefficient $r_m$ and translates it by the vector $\boldsymbol{\tau}=(s,t)$ to make W=$m$(M) as illustrated in Fig. 1.a.

Similarly, an ESAM is defined by $\omega=m^{-1}$ (W→M), such that:

$$\boldsymbol{x}_m = \omega(\boldsymbol{x}) = r_\omega(\boldsymbol{x} - \bar{\boldsymbol{x}}_\omega) + \bar{\boldsymbol{x}}_m \qquad (3)$$

where $r_\omega$ is the scaling coefficient of $\omega$ as follows:

$$r_\omega = r_m^{-1} > 1 \qquad (4)$$

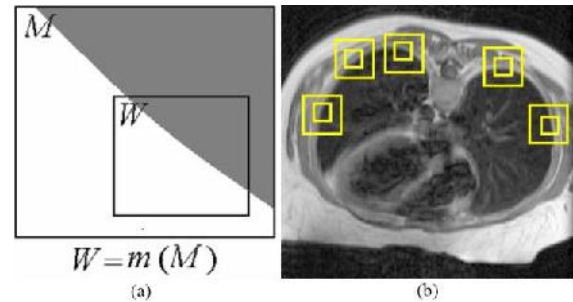Obviously, the inverse of each CSAM is an ESAM and vice versa.



**Fig. 1. (a) An example of a CSAM and (b) five optimal CSAMs allocated in a CT image of the human lunge.**

From among parameters of self-affine map, only $s$ and $t$ are usually optimized by minimizing a distance function while $r_m$ and $r_\omega$ are kept constant to reduce the computation burden [44-46, 48]. In more detail, the process of allocating self-affine maps includes two steps. First, some patches (M or W) are specified based

on the problem demands. Then, in each step of the matching algorithm, the value of every parameter is changed to compute the following cost function [41]:

$$e_W(\tau) = \frac{1}{2} \iint_{x \in W} (I(x) - I(x_m))^2 \, dx \, dy \qquad (5)$$

After checking all possible situations, the globally optimal translation vector (GOTV) of $e_W$ is obtained as follows:

$$\tilde{\tau} = \text{index}\left(\min_{-k<s,t<k}(e_W(\tau))\right); \quad k = \frac{\mu}{2} \qquad (6)$$

where the possible values of $s$ and $t$ are chosen in the range of $[-k,k]$, $\mu$ indicates the size of square domain-patches, and $\tilde{\tau} = (\tilde{s}, \tilde{t})$ is the optimal translation vector.

The dual of $e_W$ can be obtained by substituting $x$ with $m(x)$ as follows:

$$e_M(\tau) = \frac{1}{2} \iint_{x \in M} (I(x) - I(x_\omega))^2 \, dx \, dy \qquad (7)$$

such that,

$$e_M(\tau) = r_\omega^2 \, e_W(\tau) \qquad (8)$$

Obviously, both $e_W$ and $e_M$ include the same extremums.

Fig. 1 illustrates five CSAMs with $r_m$=0.5. As shown, the texture of each larger domain-patch is almost similar to that of the corresponding smaller range-patch. Furthermore, five benchmark domain patches that we used in this paper to analytically study the properties of self-affine maps are shown in Fig. 2.

Hereafter, the paper is mostly focused to study CSAM properties. Similar results can be obtained for ESAMs in the same manner, by replacing M, W, $m$, $\omega$, and $r_m$ with W, M, $\omega$, $m$, and $r_\omega$, respectively.

## 2.2. Relation to Mumford-Shah Functional

The Mumford-Shah functional for image segmentation [49] is defined by:

$$f(u,\Gamma) = \lambda_1 \int_{\hat{\Omega}} |I(x) - \hat{I}(x)|^2 \, dx \, dy +$$

$$\int_{\hat{\Omega} - \Gamma} |\nabla \hat{I}(x)|^2 \, dx \, dy +$$

$$\lambda_2 \cdot \text{Length}(\Gamma) \qquad (9)$$

where $\lambda_1$ and $\lambda_2$ are positive parameters. By minimizing this functional, the piecewise smoothed image $\hat{I} : \hat{\Omega} \rightarrow [0,1]$ ($\hat{\Omega} \subseteq \Omega$) is obtained which includes smoothed regions separated by sharp boundaries (indicated by $\Gamma$). For more details, in the above equation, the first term ensures $\hat{I}$ to stay close to $I$ while the second term smoothes the solution. Finally, the last term minimizes the total length of boundaries.

Assume that we define $\hat{\Omega} = W$ and $\hat{I}(x) = I(x_m)$ for a CSAM. Therefore, according to the above

equation, $\tau$ should be optimized such that $\hat{I}(W)$ provides the best approximation of $I(W)$. However, M does not depend on $\tau$, because it is initially allocated and remains unchanged during the matching process (see Section 2). Accordingly, $\hat{I}$ and $\Gamma$ are also fixed due to $\hat{I}(W) = I(\omega(W)) = I(M)$. Hence, the second and last terms of Eqn. (9) are independent of $\tau$ and the above functional can be simplified as follows:

$$f(\tau) = c + \lambda_1 \iint_{x \in W} |I(x) - I(x_m)|^2 \, dx \, dy \qquad (10)$$

Obviously, the positive constants $c$ and $\lambda_1$ do not affect the extremums of $f$. Thus, for CSAMs, the Mumford-Shah functional can be further simplified to the cost function of Eqn. (5).

## 2.3. Obvious Solution

The gradient of $e_W$ with respect to $\tau$ is given by:

$$\hat{\nabla} e_W(\tau) = r_\omega \iint_{x \in W} (I(x) - I(x_m)) \nabla I(x_m) \, dx \, dy$$

$$(11)$$

where $\nabla = \frac{\partial}{\partial x}$ and $\hat{\nabla} = \frac{\partial}{\partial \tau}$ are two gradient operators. Local minima of $e_W$ can be obtained by solving the following equation:

$$\left\| \hat{\nabla} e_W(\tilde{\tau}) \right\| = 0 \qquad (12)$$

where $\tilde{\tau} = (\tilde{s}, \tilde{t})$ indicates a LOTV of $e_W$ (Obviously, each GOTV is a root of the above equation as well). As maintained by the triangular inequality [50], we have:

$$0 \le \left\| \hat{\nabla} e_W(\tau) \right\| \le r_\omega \iint_{x \in W} |I(x) - I(x_m)| \cdot \|\nabla I(x_m)\| \, dx \, dy$$

$$(13)$$

where $\| \cdot \|$ is Minkowski's distance of the second rank [51]. According to the sandwich theorem [49], the roots of the right term of Eqn. (13) are also the solutions of Eqn. (12). Therefore, we can obtain some solutions of Eqn. (12) by solving the following equation:

$$\iint_{x \in W} |I(x) - I(x_m)| \cdot \|\nabla I(x_m)\| \, dx \, dy = 0 \qquad (14)$$

The optimal answers of the above equation should satisfy the following conditions:

$$\forall x \in W: \begin{cases} \text{(I)} & \|\nabla I(x_m)\| = 0 \\ \text{or} \\ \text{(II)} & I(x_m) = I(x) \end{cases} \qquad (15)$$

The first condition usually is fulfilled in the smoothed regions of the image. Therefore, each translation vector which observes the following constraint for every edge component of M determines a LOTV:
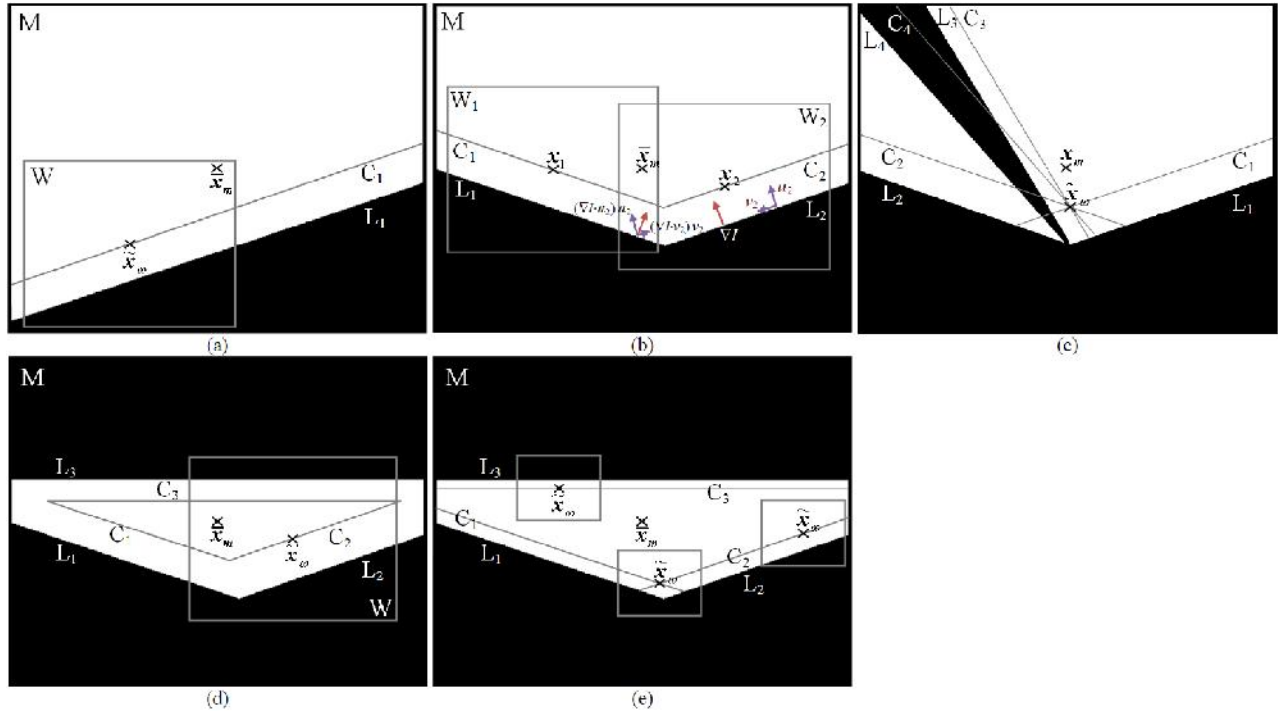
**Fig. 2. Five benchmark domain patches used to analytically study properties of self-affine maps. M includes (a) only one edge-segment (*i.e.* $L_1$), (b) two intersecting edge-segments (*i.e.* $L_1$ and $L_2$); (c) four convergent edge-segments (*i.e.* $L_1$ to $L_4$); and (d), (e) three non-convergent edge-segments (*i.e.* $L_1$ to $L_3$) with $r=0.5$ and $r=0.2$, respectively.**

$$\forall \boldsymbol{x}_m \in \mathrm{M}, \ \delta < \left\| \nabla I(\boldsymbol{x}_m) \right\|: \ I(\boldsymbol{x}) = I(\boldsymbol{x}_m) \qquad (16)$$

where $\delta$ is a small positive threshold and $\boldsymbol{x} = m(\boldsymbol{x}_m) \in \mathrm{W}$. A general solution of Eqn. (6) can be given by:

$$\forall \boldsymbol{x}_m \in \mathrm{M}: \quad \boldsymbol{x} = \boldsymbol{x}_m$$
$$\Rightarrow \boldsymbol{x} = r_\omega (\boldsymbol{x} - \overline{\boldsymbol{x}}_\omega) + \overline{\boldsymbol{x}}_\omega - \widetilde{\boldsymbol{\tau}} \qquad (17)$$
$$\Rightarrow \widetilde{\boldsymbol{\tau}} = r_\omega (1 - r_m)(\boldsymbol{x} - \overline{\boldsymbol{x}}_\omega)$$

Because $\widetilde{\boldsymbol{\tau}}$ should be independent of $\boldsymbol{x}$, we can write:

$$r_m = r_\omega = 1 \Rightarrow \widetilde{\boldsymbol{\tau}} = \boldsymbol{0} \qquad (18)$$

However, this obvious solution is disadvantageous because of reducing the self-affine map to the identical map.

Computing the solutions of Eqn. (6) in the general form is too complicated and may be useless. Thus, let the domain-patch of any CSAM be PC [29]. Thus, it consists of distinct smoothed regions separated by sharp boundaries (*e.g.* step edges). These constraints are usually observed when the size of M is small enough although we will lessen them in the sequel.

## 2.4. Global Zero-Minima

This section exhaustively studies global minima of the self-affine cost function with $e_\mathrm{W}=0$ (phrasally, referred to as the global zero-minima). First, for a domain-patch

with only one edge-segment, the locus of global zero-minima is obtained and the attracting and repelling behaviors are investigated. Next, results are extended the domain patch with some convergent edge-segments. Finally, we sum all consequences up in Theorem 1.

### 2.4.1. One Edge-Segment

Suppose that in a CSAM, M includes only one edge-segment as follows:

$$\mathrm{L}_i = \left\{ \boldsymbol{x} \in \mathrm{M} \middle| y = a_i x + b_i \right\}, \quad i = 1, 2, \ldots, n_\mathrm{M} \qquad (19)$$

where $n_\mathrm{M}$ is the total number of edge-segments within M (here, $n_\mathrm{M}=1$). This line divides M into two separate regions (*e.g.* see Fig. 2.a). For all components of M except those on $\mathrm{L}_i$, we have:

$$\forall \boldsymbol{x}_m \notin \mathrm{L}_i: \quad \left\| \nabla I(\boldsymbol{x}_m) \right\| = 0 \qquad (20)$$

In this case, the constraint of Eqn. (16) will take place if, and only if, both the original and mapped components are located on the same edge-segment as follows:

$$\boldsymbol{x}_m, \boldsymbol{x} = m(\boldsymbol{x}_m) \in \mathrm{L}_i \Rightarrow \begin{cases} y = a_i x + b_i \\ y_m = a_i x_m + b_i \end{cases} \qquad (21)$$

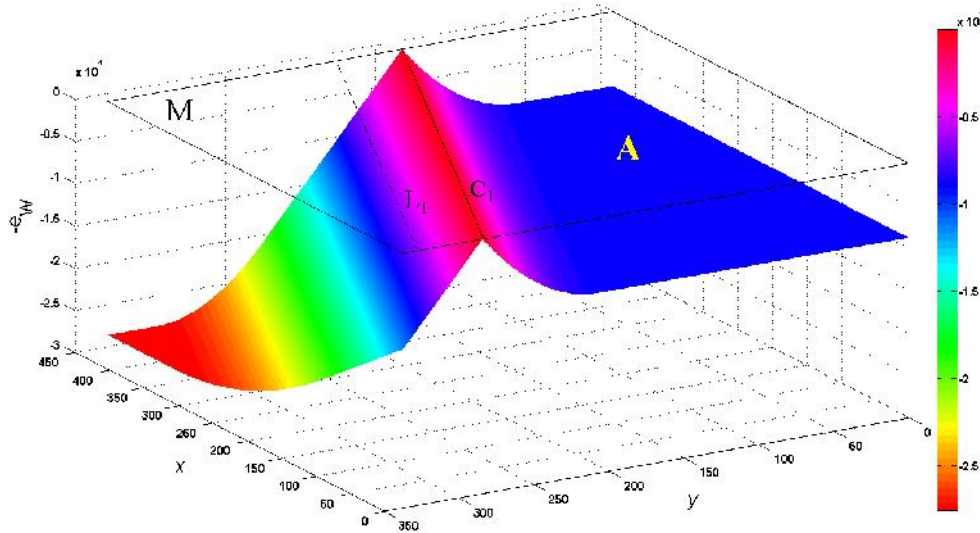where $\boldsymbol{x}=(x,y)$ and $\boldsymbol{x}_m=(x_m,y_m)$. Hence, by using Eqns. (1) and (2), we can write:

**Fig. 3. Variations of $-e_W$ versus different W-centers within M for the CSAM of Fig 2.a whose domain patch includes only one edge-segment.**

$$\left(r_m(y_m - \bar{y}_m) + \bar{y}_m + \tilde{t}\right) =$$
$$a_i\left(r_m(x_m - \bar{x}_m) + \bar{x}_m + \tilde{s}\right) + b_i \Rightarrow$$

$$b_i = y_m - a_i x_m =$$
$$\frac{1}{r_m}\left((1-r_m)(a_i \bar{x}_m - \bar{y}_m) + (a_i\tilde{s} - \tilde{t}) + b_i\right) \Rightarrow$$

$$\tilde{t} = a_i\tilde{s} - (1-r_m)(\bar{y}_m - a_i\bar{x}_m - b_i)$$

(22)

Therefore, the locus-line of optimal translation vectors (LLT) can be given by:

$$T_i = \left\{ \underset{-k<\tilde{s},\tilde{t}<k}{\tilde{\boldsymbol{\tau}} = (\tilde{s}, \tilde{t})} \middle| \tilde{t} = a_i\tilde{s} - (1-r_m)(\bar{y}_m - a_i\bar{x}_m - b_i) \right\}$$

(23)

such that,

$$\forall \tilde{\boldsymbol{\tau}} \in T_i : \quad \left\| \hat{\nabla} e_W(\tilde{\boldsymbol{\tau}}) \right\| = 0$$

(24)

Equivalently, locus-line of optimal W-centers (LLW) is obtained by:

$$C_i = \left\{ \tilde{\boldsymbol{x}}_\omega = (\tilde{x}_\omega, \tilde{y}_\omega) \middle| \tilde{\boldsymbol{x}}_\omega \in M, \ \tilde{y}_\omega = a_i\tilde{x}_\omega + \hat{b}_i \right\}$$

(25)

where $\tilde{\boldsymbol{x}}_\omega$ is a locally optimal W-center (LOWC) and $\hat{b}_i$ is computed as follows:

$$\hat{b}_i = b_i + r_m(\bar{y}_m - a_i\bar{x}_m - b_i)$$

(26)

The second term of the above equation will vanish, if $L_i$ passes through $\bar{x}_m$. In this case, $C_i$ completely fits to $L_i$. Furthermore, there is a one-to-one match between $T_i$ and $C_i$ (because of $\tilde{\boldsymbol{x}}_\omega = \bar{\boldsymbol{x}}_m + \tilde{\boldsymbol{\tau}}$) while both are parallel to $L_i$ with the same slope of $a_i$. Thus, hereafter, we may use each instead of the other.

In the above CSAM, for each LOWC on $C_i$, every component of M is mapped to another component on the same side of $L_i$ (it will be further justified in the next section). Therefore, we can write:

$$\forall \tilde{\boldsymbol{\tau}} \in T_i : \quad \left\| e_W(\tilde{\boldsymbol{\tau}}) \right\| = 0$$

(27)

Thus, every component of $T_i$ actually indicates a GOTV with zero cost value (or phrasally, G0TV). Similarly, each component of $C_i$ is a globally optimal W-center (GOWC) with zero cost value (or phrasally, G0WC). The above discussion can be summarized by the following lemma.

**Lemma 1.** *Assume that in a CSAM, the domain-patch M is PC and includes only one edge-segment. First, there is a general one-to-one match between G0TVs and G0WCs. Second, the loci of G0TVs and G0WCs are two lines, parallel to the edge-segment and given by Eqns. (23) and (25), respectively.*

For example, Fig. 3 illustrates variations of $-e_W$ versus different W-centers for the CSAM of Fig. 2.a whose domain patch includes only one edge-segment. Clearly, all G0WCs are located on $C_1$ which is also parallel to $L_1$. It also implies that by using the original cost function formulation of Eqn. (5), a self-affine map may have a number of equivalent optimal solutions (see Section 8).

Let the function $\phi_i(\boldsymbol{x})$ compute the algebraic distance of $\boldsymbol{x}$ from the line $L_i$ as follows:

$$\phi_i(\boldsymbol{x}) = y - a_i x - b_i$$

(28)

Obviously, the Euclidian distance is given by:

$$\Phi_i(\boldsymbol{x}) = \frac{|\phi_i(\boldsymbol{x})|}{\sqrt{1 + a_i^2}}$$

(29)

By using some algebraic manipulations, for any CSAM, we can write:

$$\forall \boldsymbol{x} \in M : \quad \phi_i(\boldsymbol{x}_\omega) = r_m \phi_i(\boldsymbol{x}) + \left(\phi_i(\bar{\boldsymbol{x}}_\omega) - r_m \phi_i(\bar{\boldsymbol{x}}_m)\right)$$

(30)

$$\forall \boldsymbol{x} \in W : \quad \phi_i(\boldsymbol{x}) = r_m \phi_i(\boldsymbol{x}_m) + \left(\phi_i(\bar{\boldsymbol{x}}_\omega) - r_m \phi_i(\bar{\boldsymbol{x}}_m)\right)$$
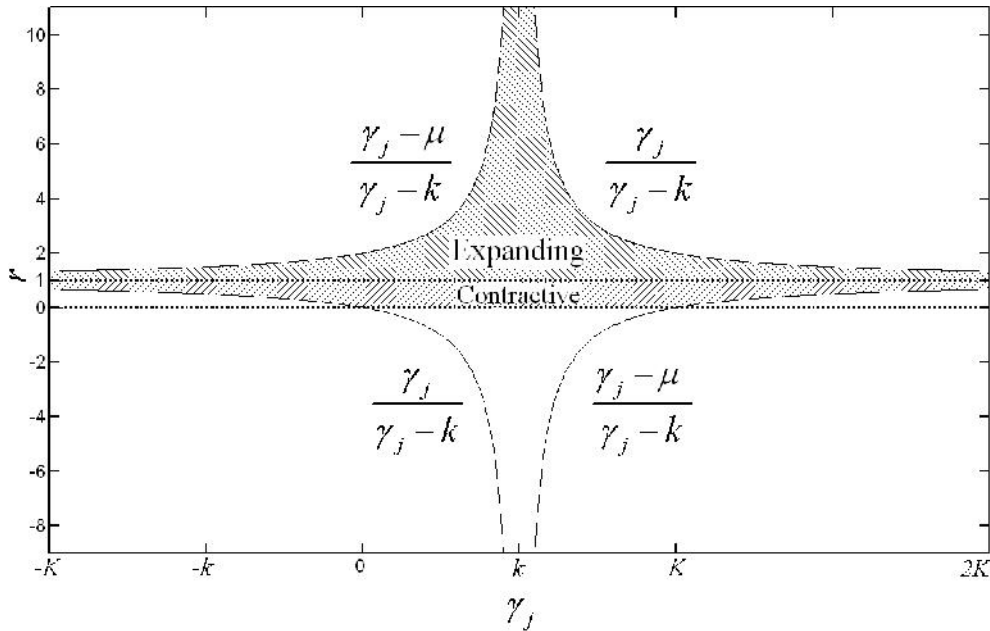
(31)

**Fig. 4.** Range of acceptable values of $r_m$ ($r<1$) and $r_\omega$ ($1<r$) versus different values of $\gamma_j$ when M **includes two edge-segments.**

In the right side of the above equations, the second term vanishes for each G0WC (*i.e.* $\overline{x}_\omega = \widetilde{x}_\omega$); and consequently, they can be simplified as follows:

$$\forall x \in \mathrm{M}: \quad \phi_i(x_\omega) = r_m\,\phi_i(x) \tag{32}$$

$$\forall x \in \mathrm{W}: \quad \phi_i(x) = r_m\,\phi_i(x_m) \tag{33}$$

Therefore, once each component of M ( $x \in \mathrm{M}$ ) is mapped by an optimal CSAM, its distance to $\mathrm{L}_i$ is decreased by the coefficient $r_m$. On the other hand, in this case, the signs of $\phi_i(x)$, $\phi_i(x_\omega)$, and $\phi_i(x_m)$ remain the same which means that $x$, $x_\omega$, and $x_m$ are located at the same side of $\mathrm{L}_i$ (it further justifies Eqn. 27). Finally, the above discussion can be summarized by the following lemma.

**Lemma 2.** *For each G0WC given by Lemma 1, the CSAM supports the attracting behavior; such that once every component of* M *is mapped through m (Eqn. 1), its distance to the edge-segment within* M *is decreased by the coefficient $r_m$.*

Note that the repelling behavior of ESAMs can be proved by the same manner (see Section 2).

### 2.4.2. Some Convergent Edge-Segments

Assume that in a CSAM, M include $n_\mathrm{M}>1$ edge-segments (see Eqn. 19). For each $\mathrm{L}_i$, the corresponding LLW ( *i.e.* $\mathrm{C}_i$) is given by Eqn. (25). Suppose all LLWs intersect at the same cross-point within M (*e.g.* see Figs. 2.b and 2.c) which is given by solving the following equations set:

$$\begin{cases} \mathrm{C}_1: & \widetilde{y}_\omega = a_1\widetilde{x}_\omega + \hat{b}_1 \\ \mathrm{C}_2: & \widetilde{y}_\omega = a_2\widetilde{x}_\omega + \hat{b}_2 \\ \vdots \\ \mathrm{C}_{n_\mathrm{M}}: & \widetilde{y}_\omega = a_{n_\mathrm{M}}\widetilde{x}_\omega + \hat{b}_{n_\mathrm{M}} \end{cases} \tag{34}$$

This cross-point provides a unique G0WC, because it separately satisfies all constraints of Lemma 1 for each edge-segment. Here, we prove that when all edge-segments are convergent, the corresponding LLWs are also convergent and vice versa.

Let's $\widetilde{x}_m$ be the cross-point of all edge-segments. Thus, we can write:

$$\forall i = 1,2,\ldots, n_\mathrm{M}: \quad \phi_i(\widetilde{x}_m) = 0 \tag{35}$$

Once the W-center is on $\mathrm{C}_i$, all components of $\mathrm{L}_i$ are mapped to themselves (see Lemmas 1 and 2). To separately confirm the above condition for each edge-segment, the optimal W-center should be chosen such that $\widetilde{x}_m$ is mapped to itself as follows:

$$\forall i = 1,2,\ldots, n_\mathrm{M}: \quad \widetilde{x}_m = m_i(\widetilde{x}_m) \tag{36}$$

Hence, by using some algebraic manipulations, we can obtain:

$$\widetilde{x}_\omega = r_m\,\overline{x}_m + (1 - r_m)\widetilde{x}_m \tag{37}$$

Generally, the unique optimal W-center $\widetilde{x}_\omega$ is obtained as a weighted sum of $\widetilde{x}_m$ and $\overline{x}_m$. Therefore, all corresponding LLWs intersect at $\widetilde{x}_\omega$ as well.

In practice, we usually tend to keep $\widetilde{x}_m$ within M which can be achieved via the following constraints (see Eqns. 6 and 23):

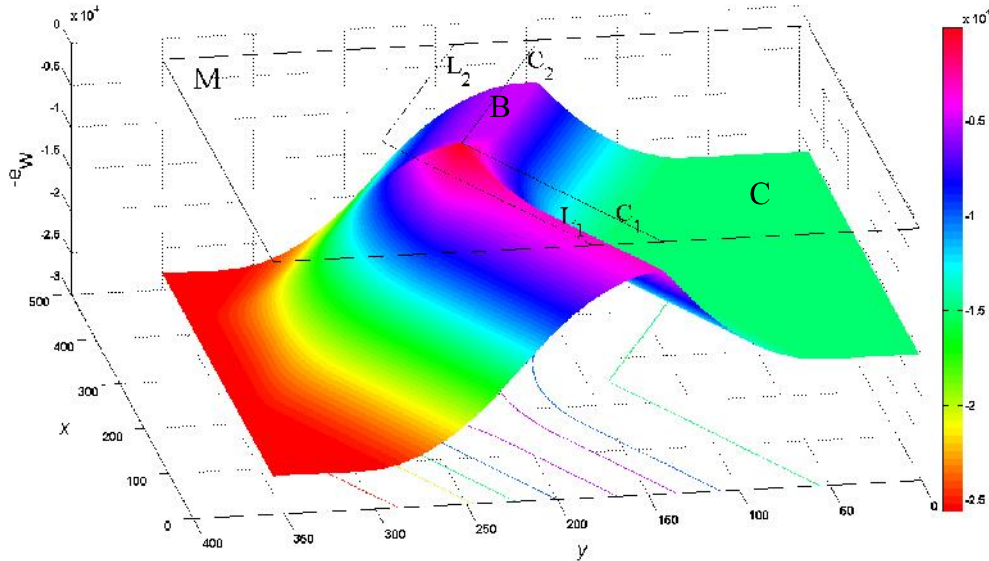$$-k < \widetilde{s}, \widetilde{t} < k \tag{38}$$

**Fig. 5. Variations of** $-e_W$ **versus different W-centers within** M **for the CSAM of Fig 2.b whose domain patch includes two intersecting edge-segments.**

Particularly, when M includes two intersecting edge-segments (*i.e.* $a_1 \neq a_2$), the unique G0TV is given by:

$$\begin{cases} \widetilde{s} = -(1-r_m)\left( \dfrac{b_1 - b_2}{a_1 - a_2} + \overline{x}_m \right) \\[4mm] \widetilde{t} = -(1-r_m)\left( \dfrac{a_2 b_1 - a_1 b_2}{a_1 - a_2} + \overline{y}_m \right) \end{cases} \qquad (39)$$

Considering this fact that $\overline{x} = \overline{y} = k$, we have:

$$-k < (1 - r_m)(\gamma_j - k) < k, \quad j = 1,2 \qquad (40)$$

where $\gamma_1$ and $\gamma_2$ are given by:

$$\begin{cases} \gamma_1 = \dfrac{b_1 - b_2}{a_2 - a_1} \\[4mm] \gamma_2 = \dfrac{b_1 a_2 - a_1 b_2}{a_2 - a_1} \end{cases} \qquad (41)$$

Thus, the cross-point of LLWs remains inside M, once the following constraints are fulfilled:

$$\text{CSAM}: \quad r_{\min} = \max\left( \max_{j=1,2}\left( \frac{\max(\gamma_j - \mu, -\gamma_j)}{|\gamma_j - k|} \right), 0 \right) < r_m < 1 \qquad (42)$$

$$\text{ESAM}: \quad 1 < r_\omega < r_{\max} = \max\left( \min_{j=1,2}\left( \frac{\max(\gamma_j, -(\gamma_j - \mu))}{|\gamma_j - k|} \right), 1 \right) \qquad (43)$$

Fig. 4 illustrates the range of acceptable values of $r_m$ and $r_\omega$ versus different values of $\gamma_j$. As shown, $e_W$ more probably includes a global zero-minimum when the value of $r_m$ is closer to one. This consequence is intuitively reasonable, because according to Eqns. (25) and (26), by approaching $r_m$ to one, all LLWs and, in turn, their cross-point move toward the center point of M. Therefore, even when the cross-point of edge-

segments is outside of M, the cross-point of LLWs may be within M by using an appropriate $r_m$ sufficiently close to one.

Generally, Eqns. (42) and (43) can be extended for $n_M$ edge-segments as follows:

$$\text{CSAM}: \quad r_{\min} = \max\left( \max_{p,q,j}\left( \frac{\max(\gamma_{pqj} - \mu, -\gamma_{pqj})}{|\gamma_{pqj} - k|} \right), 0 \right) < r_m < 1 \qquad (44)$$

$$\text{ESAM}: \quad 1 < r_\omega < r_{\max} = \max\left( \min_{p.q.j}\left( \frac{\max(\gamma_{pqj}, -(\gamma_{pqj} - \mu))}{|\gamma_{pqj} - k|} \right), 1 \right) \qquad (45)$$

where for the pair $(L_p, L_q)$, $\gamma_{pq1}$ and $\gamma_{pq2}$ are given by:

$$\begin{cases} \gamma_{pq1} = \dfrac{b_p - d_q}{a_q - a_p} \\[4mm] \gamma_{pq2} = \dfrac{b_p a_q - a_p d_q}{a_q - a_p} \end{cases} \qquad (46)$$

Therefore, we can sum the above discussion up in the following lemma.

**Lemma 3.** Assume that in a CSAM, the domain-patch M is PC and includes $n_M > 1$ convergent edge-segments. First, the corresponding LLWs are also convergent and second, their cross-point (given by Eqn. 37) will indicate the unique G0WC if, and only if, the constraint of Eqn. (44) takes place.

Indeed, in a self-affine map with convergent edge-segments, the cross-point of LLWs separately meets Eqns. (32) and (33) for each edge-segment. Thus, it inherits their common properties such as zero cost value and attracting (or repelling) behavior as follows.
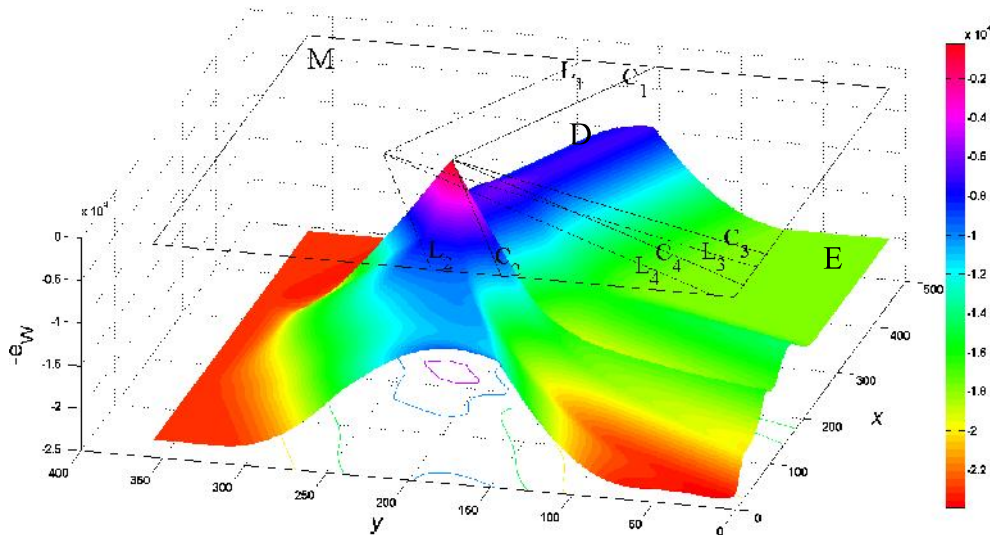
**Fig. 6. Variations of** $-e_W$ **versus different W-centers inside M for the CSAM of Fig 2.c whose domain patch includes four convergent edge-segments.**

**Lemma 4.** *For the unique G0WC given by Lemma 3, CSAM supports the attracting behavior such that once each component of M is mapped through m, its distance to each edge-segment is decreased by the coefficient $r_m$.*

Finally, we can straightforwardly extend Lemmas 1-4 to a theorem of necessary-and-sufficient conditions for global zero-minima as follows.

**Theorem 1 (Global Zero-Minima).** Assume that in a CSAM, the domain-patch M is PC. First, when M includes no edge-segment, each component of M obviously determines a G0WC. Second, once M involves only one edge-segment, every component of the attached LLW indicates a G0WC. Finally, if M includes only some convergent edge-segments, the corresponding LLWs are also convergent and their cross-point provides the unique G0WC. Furthermore, except for the first case, this CSAM usually supports the attracting behavior.

For example, Fig. 5 illustrates variations of $-e_W$ versus different W-centers for the CSAM of Fig. 2.b whose domain patch includes two intersecting edge-segments. The unique G0WC is located on the cross-point of $C_1$ and $C_2$ (referred to as $C_{(1,2)}$) given by Eqn. (37). However, $e_W$ includes a number of non-zero local minima (*e.g.* those on the inflated region specified by the label B) which cannot be handled by Theorem 1.

Another example is Fig. 6 which illustrates the results of a CSAM with four convergent edge-segments (as shown in Fig. 2.c). Again, the cross-point of LLWs determines the unique G0WC. Although Theorem 1 can successfully specify the global zero-minimum, it is silent about the local minima of the inflated and flat

regions indicated by the labels D and E, respectively, in the figure.

## 2.5. Important Local Minima

Although the main purpose of this work is computing the unique GOWC of any self-affine map, LOWCs are also important in two aspects. First, they can provide an exhaustive description of $e_W$. Second, each GOWC, actually, is a LOWC with the best cost value.

In this section, the dual of Theorem 1 is given to determine some important LOWCs of the self-affine map. For more details, in the same manner of Eqn. (11), by using Eqn. (7), we can obtain:

$$\hat{\nabla} e_M(\tau) = - \iint\limits_{x \in M} \left( I(x) - I(x_\omega) \right) \nabla I(x_\omega)\, dxdy \tag{47}$$

Thus, by replacing $x_\omega$ with $x$, we have:

$$\hat{\nabla} e_M(\tau) = r_\omega^2 \iint\limits_{x \in W} \left( I(x) - I(x_m) \right) \nabla I(x)\, dxdy \tag{48}$$

Then, using Eqn. (8), we can write:

$$\hat{\nabla} e_W(\tau) = \iint\limits_{x \in W} \left( I(x) - I(x_m) \right) \nabla I(x)\, dxdy \tag{49}$$

Finally, similar to (15), each LOWC should meet the following constraints:

$$\forall x \in W: \quad \begin{array}{ll} (I) & \|\nabla I(x)\| = 0 \\ (II) & I(x) = I(x_m) \end{array} \tag{50}$$

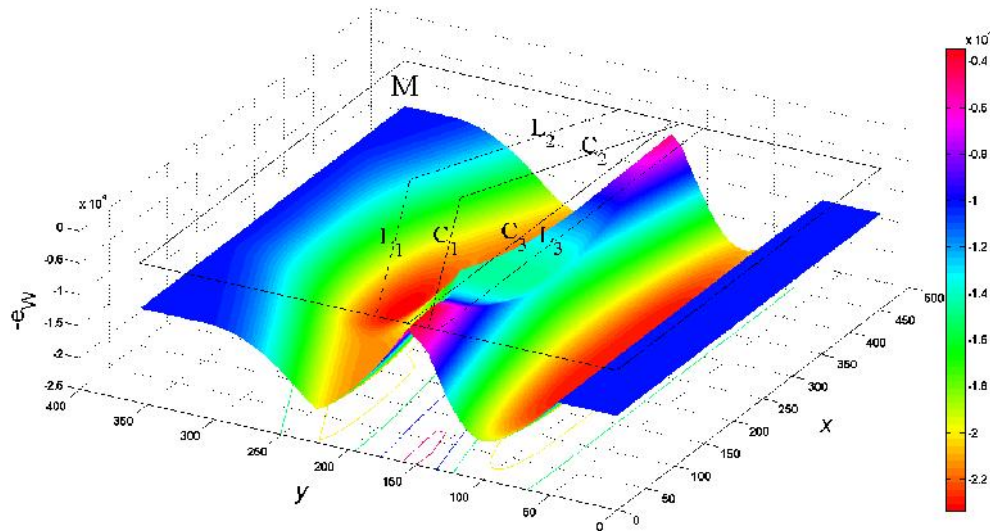Therefore, in the same manner of Theorem 1, we can obtain similar results for W instead of M as follows.

٨٥

**Fig. 7. Variations of** $-e_W$ **versus different W-centers inside** M **for the CSAM of Figs. 2.d (with** $r_m$=0.5**) whose domain patch includes three non-parallel edge-segments.**

**Theorem 2 (Important Local Minima).** Assume that in a CSAM, the range-patch W is PC. Some LOWCs can be determined as follows: first, every possible W-center for which W has no edge-segment; second, each component of the corresponding LLW once W includes only one edge-segment; and finally, the cross-point of corresponding LLWs when W (M) involves only some convergent edge-segments. Furthermore, except for the first case, this CSAM usually supports the attracting behavior.

For example, the flat regions labeled by the letters A, C, and E in Figs. 3, 5, and 6, respectively, were obtained when W included no edge-segment. Also, the inflated regions shown by the labels B and D in Figs. 3 and 5, respectively, were provided once the range-patch involves only one edge-segment.

Furthermore, according to Theorem 2, our previous assumption about piecewise constancy of M (see Section 4) can reduce to piecewise constancy of the smaller patch W. In most image processing applications of CSAMs, the size of W is small enough [44] to satisfy this constraint (*e.g.* circular range-patches with a radius of 2 pixels were used in [47]). Therefore, W usually includes no edge-segment, only one edge-segment, or some convergent edge-segments, corresponding to smoothed regions, straight edges, and typical corners, respectively. It means that for any self-affine map, there are always some LOWCs corresponding to image corners and edges which support the attracting or repelling behavior.

For example, Figs. 7 and 8 illustrate results of the CSAM whose domain patch includes three non-convergent edge-segments (see Figs. 2.d and 2.e). First, we state the results obtained with $r_m$=0.5. In this case, W usually includes a number of non-convergent edge-

segments when its center point is on every LLW, excluding some small parts next to $C_{(1,3)}$ and $C_{(2,3)}$. Although Theorem 2 has no idea for such conditions, we can maintain them by primary smoothing the image with an appropriate Gaussian kernel, especially, when the size of W is small enough.

Furthermore, one may reduce $r_m$ to decrease the probability of including non-convergent edge-segments by using a smaller W. For example, in Fig. 2.e, any range-patch W with $r_m$=0.2 usually includes either only one edge-segment or two intersecting edge-segments. Thus, every component of each LLW may denote a LOWC as further illustrated in Fig. 8.

In other words, by using a small W, the components of each LLW have more chance to be a LOWC. However, in Section 5.2, we stated that the cross-point of some convergent LLWs is more probably within M by employing a larger W. Both consequences are proper although they may seem conflicting at first glance. In more detail, when the cross-point of LLWs is not inside M due to employing a small $r_m$, every component of each LLW may indicate a LOWC according to Theorem 2. However, once they intersect at the same cross-point within M by employing a sufficiently large $r_m$, their cross-point provides a G0WC as given by Theorem 1.

## 2.6. Cost Function Improvement

In any CSAM, the center point of M is usually mapped to the W-center, *i.e.* $\overline{x}_\omega = m(\overline{x}_m)$. Thus, according to Eqn. (32), for each LOWC, we can write:

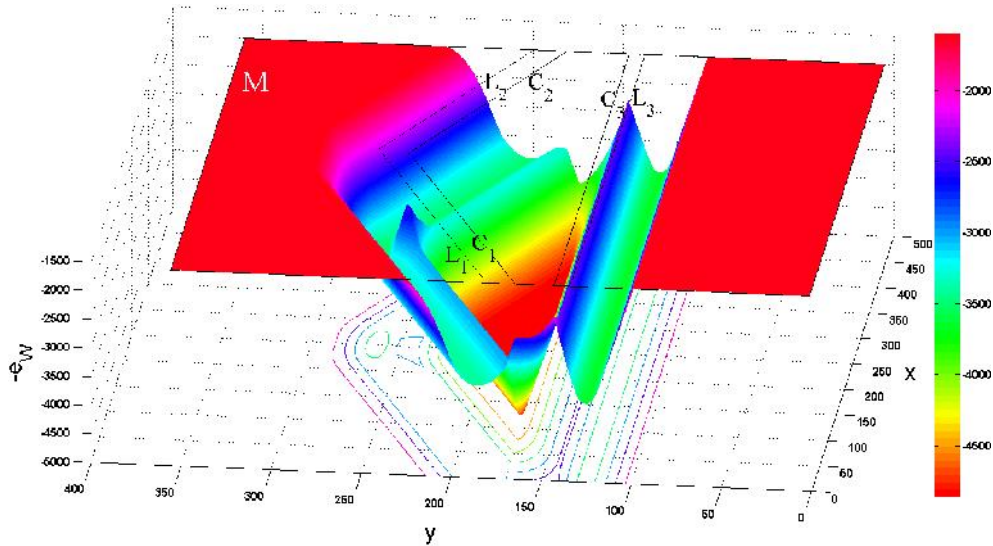$$\phi_i(\widetilde{x}_\omega) = r_m \, \phi_i(\overline{x}_m) \tag{51}$$

**Fig. 8. Variations of $-e_W$ versus different W-centers inside M for the CSAM of Figs. 2.e (with $r_m$=0.2) whose domain patch includes three non-parallel edge-segments.**

It means that compared to the center point of M, any LOWC is usually closer to edge-segments. In more detail, when M includes only one edge-segment, any GOTV usually points toward the edge-segment. Furthermore, once M involves some non-parallel edge-segments, the unique GOWC is determined by a cross-point of LLWs within M. However, this cross-point is also corresponded to a cross-point of edge-segments which indicates a corner in the image. Thus, the attached GOTV almost points toward this corner. Hence, we can draw the following lemma.

**Lemma 5 (CEP Behavior).** For any CSAM, once the given GOWC is on a LLW, the attached GOTV usually points toward a corner or an edge within M.

The authors previously used the CEP behavior to propose self-affine snake [48] in which GOTV was used to compute an external force for the parametric active contour. However, according to Theorems 1 and 2, the conventional cost function of self-affine maps (*i.e.* Eqns. 5 and 7) may provide multiple equivalent solutions, especially, when W includes no edge-segment or only one edge-segment. It is further illustrated in Fig. 9. In more detail, when M includes only one edge-segment, every point on the corresponding LLW indicates a G0WC (see Theorem 1). In turn, each G0WC is attached to a G0TV which points toward the edge-segment (see Lemma 5). Therefore, in this case, there are a number of equivalent optimal solutions for the cost function of Eqn. (5). However, may be, here, the best translation vector is the smallest one which is likely perpendicular to the edge-segment (*e.g.* the translation vector passing through the center of $W_2$ in Fig. 9).

In order to tackle the above disadvantage, we experimentally investigated the following cost function

(instead of Eqn. 7), to enhance the matching algorithm performance:

$$\hat{e}_M(\boldsymbol{\tau}) = \exp\left(-\frac{\|\boldsymbol{\tau}\|}{2k_d^2}\right)\left(1+\frac{1}{2}\iint_{\boldsymbol{x}\in M}(I(\boldsymbol{x})-I(\boldsymbol{x}_\omega))^2\,dx\,dy\right)$$

$$(52)$$

where the first term is a Gaussian kernel with STD of $k_d>0$ while the second term computes $1+e_M(\boldsymbol{\tau})$.
Obviously, the optimum translation vector can be given by:

$$\tilde{\boldsymbol{\tau}} = \text{index}\left(\min_{\boldsymbol{\tau}}(\hat{e}_M(\boldsymbol{\tau}))\right) \qquad (53)$$

Therefore, if there are some GOTVs with the same $e_M$, only the shortest one will be chosen by the above equation.
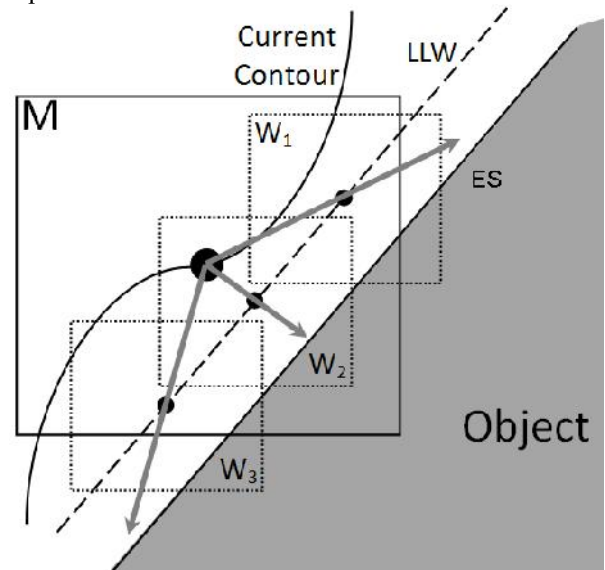


**Fig. 9. Multiple equivalent optimal solutions of CSAMs may provide uncertainty in the image processing algorithm. Here, M includes only one edge-segment while every component of the corresponding LLW determines a GOWC (*e.g.* those of $W_1$, $W_2$, and $W_3$).**

## 3. Experimental Results

To evaluate the proposed enhanced equation (Eqn. 52), it was used as the cost function of the matching algorithm (instead of Eqn. 7) in the self-affine snake [48] (with $k_d$=55). In more detail, SAS is a parametric active contour which can move/evolve in the image domain under the influence of internal and external forces [52].

The internal forces make the curve smooth while the external forces move it toward the interested features in the image. Parametric active contours are usually evolved, in light of the Euler-Lagrange formulation, by solving the following differential equation:

$$\frac{\partial x(s,t)}{\partial t} = \alpha \frac{\partial^2 x}{\partial s^2} - \beta \frac{\partial^4 x}{\partial s^4} + f_{ext} \qquad (54)$$

where $x(s,t), s \in [0,1]$ indicates the evolving curve and $f_{ext}$ is the external force.

To compute the SAS external force, in each image scale (computed by the wavelet transform), a CSAM is defined for every pixel. The external force is computed by superposition of corresponding GOTVs of different scales.

By using the proposed cost function, the performance of SAS was significantly improved. For example, Figs. 10.d and 10.e illustrate the external force fields obtained with both the conventional SAS (with Eqn. 7) and enhanced SAS (with Eqn. 55), respectively, for a synthetic image (called Room). As shown by two triangles, the uncertainty of the conventional cost function caused to appear divergent external forces close to both top-left and top-right corners of the force field. However, by using the proposed cost function, this problem is completely avoided. The evolution of the curve by using the above force fields is further illustrated in Figs. 10.b and 10.c. The divergent forces of the conventional SAS partially prevent the curve from converging to the boundary of the room shape.

As another example, Fig. 11 illustrates the results of the enhanced SAS compared to those of balloon [52], gradient vector flow (GVF) [53], generalized GVF (GGVF) [54], and active contour without edge (ACWE) [30] for a MR image of the human shoulder. This image shows the humeral head and acromion whose edges weakened or disappeared in some parts. Enhanced SAS successfully segmented the humeral head boundary while the other counterpart active contours stepped through the boundary openings.

Furthermore, as illustrated in Fig. 12, similar results were obtained for a T2 weighted MR image of the human liver. Segmentation of this medical image is really difficult, because *i)* the top-right edges of the liver are extremely weak or even disappeared in some parts (*e.g.* see the dotted ellipse); *ii)* it suffers from non-uniform brightness variations; and *iii)* the desired boundary is partially located next to stronger edges (as indicated by dotted rectangles). Again, enhanced SAS successfully segmented the liver boundary while all of the other counterpart snakes failed. In more detail, ACWE was not successful, mainly because of the non-uniform illumination changes of the liver region. Furthermore, balloon, GVF and GGVF were partially pulled out by stronger edges next to the desirable boundary while they also stepped through boundary gaps in some parts.

Finally, the corresponding total CPU times of the enhanced SAS and other counterpart snakes for two medical benchmark images illustrated in Figs. 11 and 12 are given in Table III. Although balloon provided the best CPU time, SAS converged, at least, two times faster than GGVF, and ACWE, on average.

## 4. Conclusion

Self-affine maps have been successfully used in various image processing applications such as edge detection, image segmentation, and contour extraction. All of these encouraging algorithms have been provided based on the attracting and repelling behaviors which were only experimentally investigated without any mathematical justification.

In this paper, we analytically studied important properties of self-affine maps. In more detail, it is shown that self-affine maps usually provide promising global minima in accordance with attracting or repelling behaviors. Furthermore, we proposed and proved the new CEP behavior of CSAMs. It states that each GOWC usually points toward a corner or an edge in the image.

Both of the above consequences further justified those algorithms which were previously proposed by researchers based on self-affine maps properties.

We showed that the conventional cost function of self-affine maps may have multiple equivalent optimal solutions. To avoid the uncertainty caused by this problem, a new formulation with unique optimal solution was proposed for the cost function. It was further used to improve the performance of SAS for contour extraction. Experimental results demonstrated better performance for enhanced SAS compared to the conventional SAS and a number of active contour methods.

The analytical principles given in this paper may open new horizons for researchers to present new image processing methods based on remarkable properties of self-affine maps. However, these advances are still open problems and further research is necessary to this end.

(a)                         (b)                         (c)

(d)                         (e)
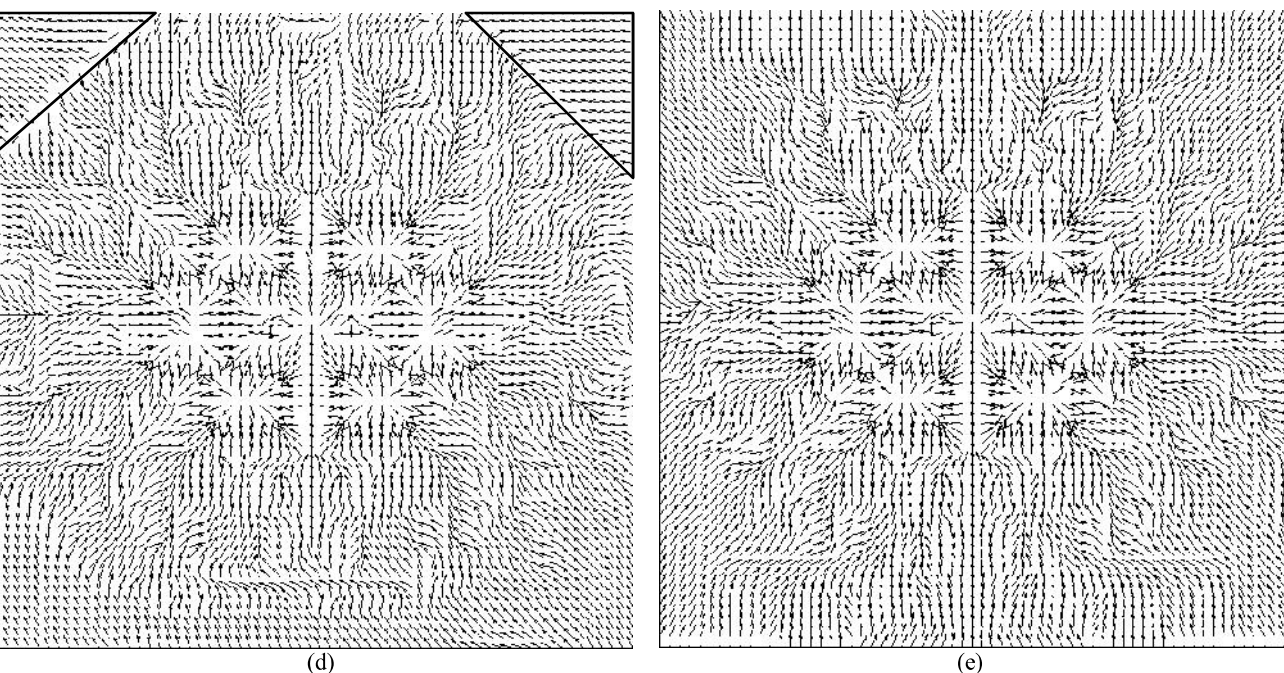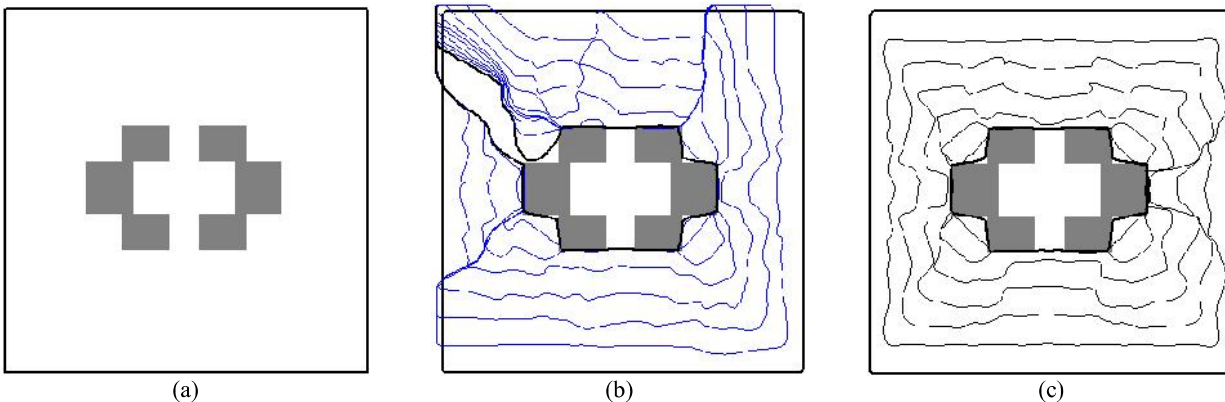
**Fig. 10. Results of the self-affine snake for a synthetic image called Room. (a) The initial contour; (b), (c) curve evolution by using (d), (e) the force fields of the conventional SAS and enhanced SAS, respectively.**

Source Image          Balloon          GGVF (GVF)        ACWE        Enhanced SAS
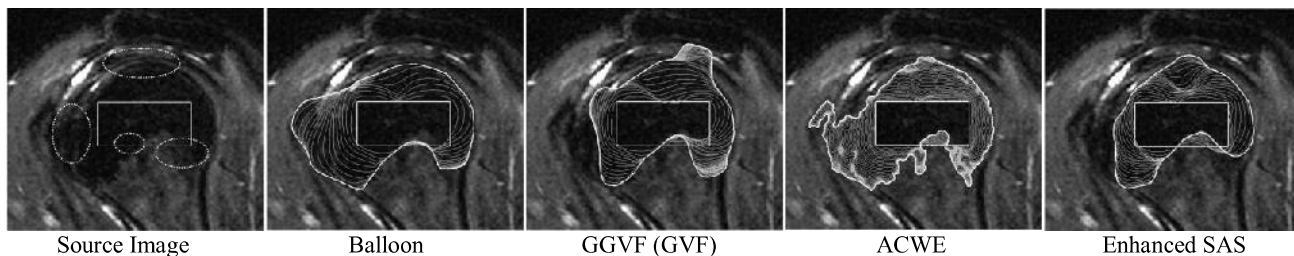
**Fig. 11. Comparing the results of enhanced SAS with those of balloon, GVF, GGVF, and CV for a sagittal oblique angulated T2 weighted MR image of the human shoulder with fat suppression. All of the counterpart algorithms used the same rectangular initial curve to evolve. As indicated by dotted ellipses in the source image, the humeral head edges have been weakened or disappeared in some parts.**

Table I. Comparing SAS with balloon, GGVF, and ACWE, in terms of CPU time, for two medical benchmark images illustrated in Figs. 11 and 12. The best results have been shown by bold-faced text.

| Medical Image | Size | Balloon | GGVF | ACWE | Enhanced SAS |
|---|---|---|---|---|---|
| Shoulder (Fig. 11) | 176×206 | **0.3** | 2.1 | 14.6 | 1.3 |
| Liver (Fig. 12) | 112×129 | **0.2** | 1.5 | 5.1 | 0.5 |
| **Average CPU Time** | | **0.3** | 1.8 | 9.9 | 0.9 |



| Source Image | Balloon | GGVF (GVF) | ACWE | Enhanced SAS |
|---|---|---|---|---|
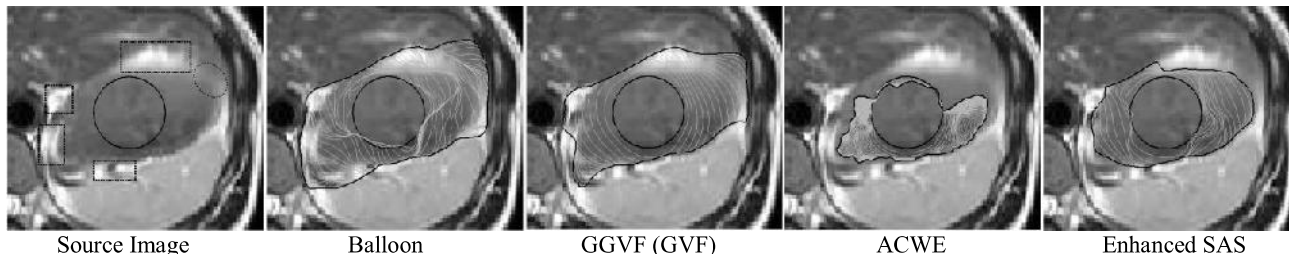
Fig. 12. Comparing the results of enhanced SAS with those of balloon, GVF, GGVF, and CV for a T2 weighted MR image of the human liver. All of the counterpart algorithms used the same circular initial curve to evolve.

# References

[1] C. Haworth, A. M. Peacock, and D. S. Renshaw, "Performance of reference block updating techniques when tracking with the block matching algorithm," IEEE Conf. Image Proc., vol. 1, pp. 365–368, 2001.

[2] T. Wiegand, G. Sullivan, G. Bjntegaard, and A. Luthra, "Overview of the H264 video coding standard," IEEE Trans. Circuits and Systems for Video Tech, vol. 13, no. 7, pp. 560–576, 2003.

[3] B. C. Song, S. C. Jeong, and Y. Choi, "Video super-resolution algorithm using bi-directional overlapped block motion compensation and on-the-fly dictionary training," IEEE Trans. Circuits and Systems for Video Technology, vol. 21, no. 3, pp. 274–285, 2011.

[4] M. Ashikhmin, "Synthesizing natural textures," Sym. Interactive 3D Graphics, pp. 217–226, 2001.

[5] L. Y. Wei and M. Levoy, "Fast texture synthesis using tree structured vector quantization," SIGGRAPH, Comp. Grap. Proc., pp. 479–488, 2000.

[6] T. S. Cho, S. Avidan, and W. T. Freeman, "The patch transform," IEEE Trans. Pattern Analysis and Machine Intelligence, vol. 32, no. 8, pp. 1489–1501, 2010.

[7] M. Ashikhmin, "Fast texture transfer," IEEE Computer Graphics and Applications, vol. 23, no. 4, pp. 38–43, 2003.

[8] A. Hertzmann, C. E. Jacobs, N. Oliver, B. Curless, and D. Salesin, "Image analogies," SIGGRAPH, Comp. Graph. Proc., pp. 327–340, 2001.

[9] A. Criminisi, P. Pérez, and K. Toyama, "Region filling and object removal by exemplar-based image inpainting," IEEE Trans. on Image Proc., vol. 13, no. 9, pp. 1200–1212, 2004.

[10] J. Hays and A. A. Efros, "Scene completion using millions of photographs," ACM Trans. Graph., vol. 26, no. 3, pp. 87–94, 2007.

[11] Z. Xu and J. Sun, "Image inpainting by patch propagation using patch sparsity," IEEE Trans. Image Processing, vol. 19, no. 5, pp. 1153–1165, 2010.

[12] C. W. Fang and J. J. J. Lien, "Rapid image completion system using multiresolution patch-based directional and nondirectional approaches," IEEE Trans. Image Processing, vol. 18, no. 12, pp. 2769–2779, 2009.

[13] S. Rashidi, A. Fallah, F. Tohidkhah, " تصدیق امضای پویا و احراز هویت مبتنی بر استخراج نقاط غالب پایدار امضا و تقطیع الگوهای ," Journal of Iranian Association of Electrical and Electronics Engineers, vol. 9, no. 1, 2012.

[14] A. Buades, B. Coll, and J. M. Morel, "A non-local algorithm for image denoising," IEEE Conf. Comp. Vision Patt. Recog., pp. 60–65, 2005.

[15] N. Azzabou, N. Paragios, F. Guichard, and F. Cao, "Variable bandwidth image denoising using image-based noise models," IEEE Conf. Computer Vision and Pattern Recognition, pp. 1–7, 2007.

[16] J. Boulanger, C. Kervrann, and P. Bouthemy, "Space-time adaptation for patch-based image sequence restoration," IEEE Trans. Patt. Anal. Mach. Intell., vol. 29, no. 6, pp. 1096–1102, 2007.

[17] T. Brox and D. Cremers, "Iterated nonlocal means for texture restoration," In Proc. 1st Int. Conf. Scale Space and Variational Methods in Computer Vision, pp.13–24, 2007.

[18] X. Li and Y. Zheng, "Patch-based video processing: a variational Bayesian approach," IEEE Trans. Circuits and Systems for Video Technology, vol. 19, no. 1, pp. 27–40, 2009.

[19] C. A. Deledalle, L. Denis, and F. Tupin, "Iterative weighted maximum likelihood denoising with probabilistic patch-based weights," IEEE Trans. Image Processing, vol. 18, no. 12, pp. 2661–2672, 2009.

[20] J. Boulanger, C. Kervrann, P. Bouthemy, P. Elbau, J. B. Sibarita and J. Salamero, "Patch-based nonlocal functional for denoising fluorescence microscopy image sequences," IEEE Trans. Medical Imaging, vol. 29, no. 2, pp. 442–454, 2010.

[21] P. Perona and J. Malik, "Scale space and edge detection using anisotropic diffusion," IEEE Trans. Patt. Anal. Mach. Intell., vol. 12, no. 7, pp. 629–639, 1990.

[22] L. Yaroslavsky, Digital Picture Processing - An Introduction. Springer Verlag, New York, 1985.

[23] S. Smith and J. Brady, "Susan - a new approach to low level image processing," Int. J. Computer Vision, vol. 23, no. 1, pp. 45–78, 1997.

[24] C. Tomasi and R. Manduchi, "Bilateral filtering for gray and color images," In Proc. 6th Int. Conf. Computer Vision, pp. 839–846, 1998.

[25] C. Kervrann and J. Boulanger, "Optimal spatial adaptation for patch-based image denoising," IEEE Trans. on Image Proc., vol. 15, no. 10, pp. 2866–2878, 2006.

[26] G. Gilboa and S. Osher, "Nonlocal linear image regularization and supervised segmentation," SIAM Multiscale Modeling and Simulation, vol. 6, no. 2, pp. 595–630, 2007.

[27] D. Tschumperlé and L. Brun, "Image denoising and registration by PDE's on the space of patches," Int. Workshop Local and Non-Local Approximation in Image Processing, 2008.

[28] S. C. Zhu and A. Yuille, "Region competition: unifying snakes, region growing, and Bayes/MDL for multiband image segmentation," IEEE Trans. Patt. Anal. Mach. Intel., vol. 18, no. 9, pp. 884–900, 1996.

[29] N. Paragios and R. Deriche, "Geodesic active regions: a new paradigm to deal with frame partition problems in computer vision," J. Visual Comm. and Image Rep., vol. 13, no. 1-2, pp. 249–268, 2002.

[30] T. F. Chan and L. A. Vese, "Active contours without edges," IEEE Trans. Image Processing, vol. 10, no. 2, pp. 266–277, 2001.

[31] X. Bresson, "Image Segmentation with Variational Active Contours," PhD Thesis, École Polytechnique Fédérale de Lausanne, p. 21, 2006.

[32] C. Li, C. Y. Kao, J. C. Gore, and Z. Ding, "Implicit active contours driven by local binary fitting energy," IEEE Conf. Computer Vision and Pattern Recognition, pp. 1–7, 2007.

[33] C. Li, C. Y. Kao, J. C. Gore, and Z. Ding, "Minimization of region-scalable fitting energy for image segmentation," IEEE Trans. Image Processing, vol. 17, no. 10, pp. 1940–1949, 2008.

[34] S. Lankton and A. Tannenbaum, "Localizing region-based active contours," IEEE Trans. Image Proc., vol. 17, no. 11, pp. 2029–2039, 2008.

[35] J. A. Yezzi, A. Tsai, and A. Willsky, "A fully global approach to image segmentation via coupled curve evolution equations," J. Vis. Comm. Image Rep., vol. 13, no. 1, pp. 195–216, 2002.

[36] O. Michailovich, Y. Rathi, and A. Tannenbaum, "Image segmentation using active contours driven by the bhattacharyya gradient flow," IEEE Trans. Image Processing, vol. 15, no. 11, pp. 2787–2801, 2007.

[37] M. Varma and A. Zisserman, "A statistical approach to material classification using image patch exemplars," IEEE Trans. Pattern Analysis and Machine Intelligence, vol. 31, no. 11, pp. 2032–2047, 2009.

[38] A. Colombari and A. Fusiello, "Patch-based background initialization in heavily cluttered video," IEEE Trans. Image Processing, vol. 19, no. 4, pp. 926–933, 2010.

[39] W. Hu, J. Xue, X. Lan, and N. Zheng, "Local patch based regularized least squares model for compression artifacts removal," IEEE Trans. Consumer Electronics, vol. 55, no. 4, pp. 2057–2065, 2009.

[40] U. Avni, H. Greenspan, E. Konen, M. Sharon, J. Goldberger, "X-ray categorization and retrieval on the organ and pathology level, using patch-based visual words," IEEE Trans. Medical Imaging, vol. 30, no. 3, pp. 733–746, 2011.

[41] M. Barnsley and L. Hurt, Fractal Image Compression. Wellesley, MA: A K Peters, 1993.

[42] D. M. Monro, F. Dudbridge, and A. Wilson, "Deterministic rendering of self-affine fractals," IEE Colloquium Application of Fractal Techniques in Image Processing, pp. 5/1–5/4, 1990.

[43] S. Kumar, K. N. Rao, R. R. Mishra, and R. C. Jain. "An efficient bath fractal transform-based image coding technique," IEEE Trans. Consumer Electronics, vol. 44, no. 4, pp. 1298–1308, 1998.

[44] T. Ida and Y. Sambonsugi, "Image segmentation and contour detection using fractal coding," IEEE Trans. Circuits Syst. Video Technol., vol. 8, no. 8, pp. 968–975, 1998.

[45] T. Ida and Y. Sambonsugi, "Self-affine mapping system and its application to object contour extraction," IEEE Trans. Image Processing, vol. 9, no. 11, pp. 1926–1936, 2000.

[46] M. Saadatmand-Tarzjan and H. Abrishami Moghaddam, "A new method for contour extraction based on self-affine mapping system," Iranian Conf. Intelligent Systems, 2004. [Online] Available: http://profdoc.um.ac.ir/paper-abstract-1030322.html

[47] M. Saadatmand-Tarzjan and H. Ghassemian, "Self-affine snake: a new parametric active contour," IEEE Int. Conf. Signal Proc. Comm., 2007.

[48] M. Saadatmand-Tarzjan and H. Ghassemian, "A novel active contour for medical image segmentation," IEICE Electronics Express, vol. 6, no. 23, pp. 1683–1689, 2009. [Online] Available: http://profdoc.um.ac.ir/paper-abstract-1030310.html

[49] D. Mumford and J. Shah, "Optimal approximation by piecewise smooth functions and associated variational problems," Commun. Pure Appl. Math, vol. 42, pp. 577–685, 1989.

[50] M. D. Greenbery, Foundation of Applied Mathematics. Prentice Hall, Englewood Cliffs, 1978.

[51] S. Theodoridis and K. Koutroumbas, Pattern Recognition. Elsevier Academic Press, San Diego, 2003.

[52] C. Xu, D. Pham, and J. L. Prince, "Image segmentation using deformable models," in Handbook of Medical Imaging. vol. 2: Medical Image Proc. and Analysis, J. Fitzpatrick and M. Sonka, Eds., London, 2000, pp. 175–272.

[53] C. Xu and J.L. Prince, "Snakes, shapes, and gradient vector flow," IEEE Trans. Image Processing, vol. 7, no. 3, pp. 359–369, 1998.

[54] C. Xu and J.L. Prince, "Generalized gradient vector flow external forces for active contours," Signal Processing, vol. 71, pp. 131–139, 1998.